On the Multiple-Relaxation-Time Micro-Flow Lattice Boltzmann Method for Complex Flows

Kazuhiko Suga[1,2] **and Takahiko Ito**[1]

Abstract: The multiple-relaxation-time lattice Boltzmann method for micro-scale flows (MRT μ-flow LBM) is extensively evaluated in this study. Following the study of Chai, Shi, Guo and Lu (2010), the diffusive bounce-back wall boundary condition and the collision matrix are modeled. To determine the model parameters, the first-order, 1.5-order and second-order slip-flow models are discussed. Since the mean free path of gas molecules is considered to be influenced by the wall in micro flow systems, the effects of a correction function after Stops (1970) are also evaluated. As the increase of the Knudsen number (Kn), it is necessary to introduce the regularization procedure to remove oscillations from the results, particularly for complex flows. The model combination thus includes the regularization procedure as well. The model validation is firstly performed in canonical force-driven Poiseuille flows at $0.01 \leq \text{Kn} \leq 10$. Then, 2-D complex flows around an obstacle such as a triangular- and a square-cylinder at $\text{Kn} \approx 0.1$ are discussed. Finally, a flow in a 3-D bumpy wall channel at $\text{Kn}=0.1$ is considered. For the 2-D and 3-D flow cases, the two dimensional nine discrete velocity (D2Q9) and the three dimensional 19 discrete velocity (D3Q19) models are applied, respectively. To describe complex shapes of wall surfaces, a linear interpolation scheme is applied to the diffusive bounce-back wall boundary condition. For providing the reference data, simulations by the molecular dynamics (MD) method using the Lennard-Jones potential are also performed for the obstacle and the bumpy channel flows. It is confirmed that the near wall correction of the molecular mean free path is important at Kn>1. With the regularization procedure, the MRT LBM reproduces the reference data very satisfactorily irrespective of the order of the slip-flow model incorporated.

Keywords: lattice Boltzmann method, micro-flow, nano-flow, molecular dynamics simulation, Poiseuille flow, obstacle flow, bumpy wall flow.

[1] Department of Mechanical Engineering, Osaka Prefecture University, Sakai, Osaka 599-8531, Japan

[2] Corresponding author: suga@me.osakafu-u.ac.jp

1   Introduction

It can be said that the lattice Boltzmann method (LBM) [e.g. McNamara and Zanetti (1988); Higuera and Jimenez (1989)] has quickly established its status in simulating fluid flows. One of the attractive features is that the LBM is particularly flexible for simulating flows in complex geometries such as flows in porous materials [Keehm, Mukerji and Nur (2004); Niu, Munekata, Hyodo and Suga (2007); Suga and Nishio (2009); Suga, Tanaka, Nishio and Murata (2009), etc.] since its algorithm is simple for treating complex flow boundaries. In fact, the LBM is now a standard approach for solving flows in engineering porous media such as those for fuel cells and catalytic converters. Although the LBM is a method to simulate Navier-Stokes flows, it is also possible to expand its applicability to flows in microsystems. There have been thus a lot of studies on the LBM for micro flows (μ-flow LBM, hereafter).

When the representative scale H of the flow geometry is in a sub-micron meter scale, since the mean free path λ of gas molecules under an atmospheric pressure becomes 0.06μm, the Knudsen number, Kn=λ/H, reaches Kn$> 10^{-2}$. Such a condition is known as the slip-flow regime and can be found in nano/micro-electro-mechanical systems. At this moderately high level of Kn, the continuum Navier-Stokes equations are no longer applicable and the Boltzmann equation (BE) of the gas kinetic theory is suitable for describing flow physics [e.g. Chapman and Cowling (1970); Cercignani (1975); Karniadakis, Beskok and Aluru (2005)]. Because of its kinetic origin, it can be naturally considered that the LBM has potential to be expanded for treating the finite Knudsen number flows. Nie, Doolen and Chen (2002), Shen, Tian, Xie and Fan (2004), Zhang, Gu, Barber and Emerson (2006) and Guo, Zhao, Shi (2006) showed promising results to describe the finite Kn flows by introducing Kn dependency into the relaxation parameter in the Bhatnagar-Gross-Krook (BGK) model [Bhatnagar, Gross and Krook (1954)] of the lattice Boltzmann equation. Succi (2002) and Sbragaglia and Succi (2005) discussed the specular-reflection and the slip-reflection effects for the wall boundary condition of the slip flow regime, respectively. Toschi and Succi (2005) introduced a virtual wall collision concept into the bounce-back and diffuse-scattering boundary conditions of Ansumali and Karlin (2002). Zhang, Qin, and Emerson (2005) applied a Maxwellian scattering kernel to the wall conditions with an accommodation coefficient.

Although most of the LBM studies, which were not only for micro flows but also for Navier-Stokes flows, were based on the single relaxation-time (SRT) BGK model, Pan, Luo and Miller (2006) reported that generally the multiple relaxation-time (MRT) model [d'Humieres, Ginzburg, Krafczyk, Lallemand and Luo (2002)] was more stable and superior to the BGK model. They showed that the SRT model had

the viscosity dependency of flows in complex porous media while the MRT improved it. (Indeed, our study on nano-mesh flows by the SRTμ-flow LBM [Suga, Takenaka, Kinjo and Hyodo (2011)] indicated that the SRT suffered from the undesirable viscosity dependency to predict the permeability in the slip and transitional flow regimes.) Accordingly, Guo, Zheng and Shi (2008) discussed the MRT method with the combination of the bounce-back and the specular reflection wall boundary condition of Succi (2002) for micro flows. In the context of the MRT LBM, Verhaeghe, Luo and Blanpain (2009) tested a diffusive bounce-back model for fully diffusive stationary walls. In our previous report [Suga and Ito (2010)], the above μ-flow MRT models by Guo, Zheng and Shi (2008) and Verhaeghe, Luo and Blanpain (2009) were evaluated in Poiseuille flows and a square cylinder flow along with the SRT μ-flow LBM. It was cofirmed that although there were still margins to improve, the MRT model was indeed superior to the SRT model and the diffusive bounce-back boundary condition was better than the combined bounce-back and specular-reflection boundary condition around a stagnation point.

Very recently, Chai, Shi, Guo and Lu (2010) considered that a possible way to improve the diffusive bounce-back boundary condition was keeping consistency with a higher order slip-flow condition of the modified Reynolds equation of tribology. They thus discussed the second-order slip-flow condition of Hadjiconstantinou (2003) to determine the model coefficients. Although they reported that capturing the Klinkenberg effect [Klinkenberg (1941)] was successful, the model performance was not sufficiently evaluated against benchmark data. Therefore, the present study extensively evaluates the effects of using several slip-flow conditions in conjunction with the other sub-models for micro flows such as the correction of the molecular mean free path and the regularization procedure. The chosen test flow cases are canonical force-driven Poiseuille flows and channel flows with an obstacle inserted. The inserted obstacle is a triangular-cylinder or a square-cylinder [Suga, Takenaka, Ito, Kaneda, Kinjo and Hyodo (2010)]. (They are referred to as the triangular- and square-cylinder flows, respectively.) Finally, as the most complicated three-dimensional (3-D) test case, a flow through a 3-D bumpy wall channel, where hemisphere bump matrices are formed, is also considered. This case is referred to as the bumpy channel flow. For 2-D and 3-D flow cases, the two dimensional nine discrete velocity (D2Q9) and the three dimensional 19 discrete velocity (D3Q19) models are applied, respectively. In order to represent the shapes of the triangular-cylinder and the bumps correctly, a linear interpolation scheme is applied to the diffusive bounce-back boundary condition. To generate the reference data for the obstacle flows and the bumpy channel flow, molecular dynamics (MD) simulations [e.g. Koplik and Banavar (1995); Haile(1997)] are performed in the present study.

2 The MRT μ-flow Lattice Boltzmann Method

Although one should refer to some of the original papers for the detailed derivation of the lattice Boltzmann equations and their modeling steps for applying to micro flows, brief descriptions are given below.

2.1 Multiple relaxation time method

The lattice Boltzmann equation can be obtained by discretizing the velocity space of the Boltzmann equation into a finite number of discrete velocities $\xi_\alpha \{\alpha = 0, 1, \cdots, Q-1\}$. Although many techniques to discretize the velocity space have been proposed, in the present study, as shown in Fig.1, the two-dimensional nine velocity (D2Q9) and three-dimensional nineteen velocity (D3Q19) models are chosen for 2-D and 3-D flows, respectively. They are the second-order accurate discrete velocity models and easily applicable to complex flow geometries. From an engineering view point, the third- or higher-order discrete velocity models are not practical since they require more than two lattice levels for the streaming. The MRT LBM [d'Humieres, Ginzburg, Krafczyk, Lallemand and Luo (2002)] transforms the distribution function $\mathbf{f}(\mathbf{x}, t)$ at the lattice site $\mathbf{x}$ at time t in the velocity space to the moment space by a transformation matrix $\mathbf{M}$. Since the moments of the distribution function correspond directly to flow quantities, the moment representation allows us to perform the relaxation processes with different relaxation-times according to different time-scales of various physical processes. The evolution equation is thus written as

$$\frac{1}{\delta t}\left[|\mathbf{f}(\mathbf{x} + \xi_\alpha \delta t, t + \delta t)\rangle - |\mathbf{f}(\mathbf{x}, t)\rangle\right] = -\mathbf{M}^{-1}\widehat{\mathbf{S}}\left[|\mathbf{m}(\mathbf{x}, t)\rangle - |\mathbf{m}^{eq}(\mathbf{x}, t)\rangle\right] + |\mathbf{F}\rangle, \quad (1)$$

where the bracketed vector such as $|\mathbf{f}\rangle$ is $|\mathbf{f}\rangle := (f_0, f_1, \cdots, f_{Q-1})^T$ and δt is the time step. The term $\mathbf{F}$ is an external body force:

$$\mathbf{F} := (F_0, F_1, \cdots, F_{Q-1}), \ F_\alpha = 3\omega_\alpha \rho_0 \frac{\xi_\alpha \cdot \mathbf{a}}{c^2}, \quad (2)$$

where $\mathbf{a}$ is the acceleration vector, $c = \delta x/\delta t$, δx is the lattice space and ρ_0 is the mean density of the system which is set to be unity. In the D2Q9 and D3Q19 models, the discrete velocity vectors are respectively

$$\xi_\alpha = \begin{cases} (0,0), & \alpha = 0, \\ (\pm 1, 0), (0, \pm 1), & \alpha = 1-4, \\ (\pm 1, \pm 1), & \alpha = 5-8, \end{cases} \quad (3)$$

$$\boldsymbol{\xi}_\alpha = \begin{cases} (0,0,0), & \alpha = 0, \\ (\pm 1,0,0),(0,\pm 1,0),(0,0,\pm 1), & \alpha = 1-6, \\ (\pm 1,\pm 1,0),(\pm 1,0,\pm 1),(0,\pm 1,\pm 1), & \alpha = 7-18. \end{cases} \quad (4)$$

The weight parameters are

$$\omega_\alpha = \begin{cases} 4/9, & \alpha = 0, \\ 1/9, & \alpha = 1-4, \\ 1/36, & \alpha = 5-8, \end{cases} \quad (5)$$
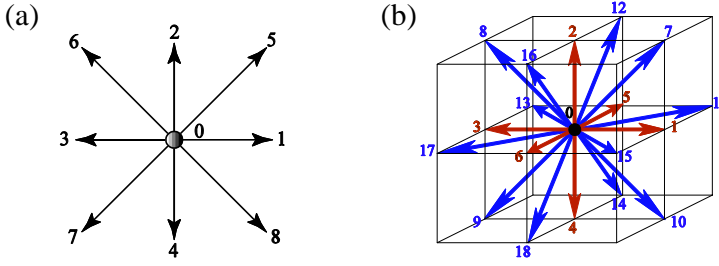

Figure 1: Discrete velocity models; (a) two-dimensional nine velocity (D2Q9) model, (b) three-dimensional nineteen velocity (D3Q19) model.

$$\omega_\alpha = \begin{cases} 1/3, & \alpha = 0, \\ 1/18, & \alpha = 1-6, \\ 1/36, & \alpha = 7-18, \end{cases} \quad (6)$$

respectively for the D2Q9 and D3Q19 models.

The fluid macro density ρ, velocity $\mathbf{u}$ and the pressure p are respectively obtained by applying the integral of microscopic velocity moment as

$$\rho = \sum_{\alpha=0}^{Q-1} f_\alpha, \ \rho\mathbf{u} = \sum_{\alpha=0}^{Q-1} f_\alpha\boldsymbol{\xi}_\alpha + \frac{\delta t}{2}\mathbf{a}, \ p = \rho c_s^2, \quad (7)$$

where the sound speed $c_s = \sqrt{RT}$ is equal to $\sqrt{1/3}$ in the D2Q9 and D3Q19 models. Here, R and T are the ideal gas constant and temperature, respectively.

The matrix $\mathbf{M}$ is a $Q \times Q$ matrix which linearly transforms the distribution function to the velocity moment: $|\mathbf{m}\rangle = \mathbf{M} \cdot |\mathbf{f}\rangle$.

For the D2Q9 model, the transformation matrix is

$$\mathbf{M} = \begin{pmatrix} 1 & 1 & 1 & 1 & 1 & 1 & 1 & 1 & 1 \\ -4 & -1 & -1 & -1 & -1 & 2 & 2 & 2 & 2 \\ 4 & -2 & -2 & -2 & -2 & 1 & 1 & 1 & 1 \\ 0 & 1 & 0 & -1 & 0 & 1 & -1 & -1 & 1 \\ 0 & -2 & 0 & 2 & 0 & 1 & -1 & -1 & 1 \\ 0 & 0 & 1 & 0 & -1 & 1 & 1 & -1 & -1 \\ 0 & 0 & -2 & 0 & 2 & 1 & 1 & -1 & -1 \\ 0 & 1 & -1 & 1 & -1 & 0 & 0 & 0 & 0 \\ 0 & 0 & 0 & 0 & 0 & 1 & -1 & 1 & -1 \end{pmatrix}. \tag{8}$$

The collision matrix $\widehat{\mathbf{S}}$ is diagonal:

$$\widehat{\mathbf{S}} = diag(s_0, s_1, \cdots, s_{Q-1}). \tag{9}$$

The moment components have physical significances:

$$|\mathbf{m}\rangle = (m_0, m_1, \cdots, m_{Q-1})^T = (\rho, e, \varepsilon, j_x, q_x, j_y, q_y, p_{xx}, p_{xy})^T, \tag{10}$$

where the density ρ and the momentum $\mathbf{j} := \rho\mathbf{u} = (j_x, j_y)$ are conserved moments. The other six non-conserved moments, e, ε, $\mathbf{q} := (q_x, q_y)$, p_{xx} and p_{xy} are, respectively, related to the energy, the energy square, the energy flux, the diagonal and off-diagonal components of the stress tensor. The equilibria of the conserved moments are themselves and those of the non-conserved moments are products of the conserved moments:

$$m_0^{eq} = \rho, \ m_1^{eq} = e^{eq} = 3\mathbf{j} \cdot \mathbf{j} - 2\rho, \ m_2^{eq} = \varepsilon^{eq} = \rho - 3\mathbf{j} \cdot \mathbf{j}, \ m_3^{eq} = j_x, m_4^{eq} = q_x^{eq} = -j_x, \tag{11}$$

$$m_5^{eq} = j_y, \ m_6^{eq} = q_y^{eq} = -j_y, m_7^{eq} = p_{xx}^{eq} = j_x^2 - j_y^2, \ m_8^{eq} = p_{xy}^{eq} = j_x j_y. \tag{12}$$

For the D3Q19 model, the transformation matrix is

$$
\mathbf{M} = \begin{pmatrix}
1 & 1 & 1 & 1 & 1 & 1 & 1 & 1 & 1 & 1 & 1 & 1 & 1 & 1 & 1 & 1 & 1 & 1 & 1 \\
-30 & -11 & -11 & -11 & -11 & -11 & -11 & 8 & 8 & 8 & 8 & 8 & 8 & 8 & 8 & 8 & 8 & 8 & 8 \\
12 & -4 & -4 & -4 & -4 & -4 & -4 & 1 & 1 & 1 & 1 & 1 & 1 & 1 & 1 & 1 & 1 & 1 & 1 \\
0 & 1 & -1 & 0 & 0 & 0 & 0 & 1 & -1 & 1 & -1 & 1 & -1 & 1 & -1 & 0 & 0 & 0 & 0 \\
0 & -4 & 4 & 0 & 0 & 0 & 0 & 1 & -1 & 1 & -1 & 1 & -1 & 1 & -1 & 0 & 0 & 0 & 0 \\
0 & 0 & 0 & 1 & -1 & 0 & 0 & 1 & 1 & -1 & -1 & 0 & 0 & 0 & 0 & 1 & -1 & 1 & -1 \\
0 & 0 & 0 & -4 & 4 & 0 & 0 & 1 & 1 & -1 & -1 & 0 & 0 & 0 & 0 & 1 & -1 & 1 & -1 \\
0 & 0 & 0 & 0 & 0 & 1 & -1 & 0 & 0 & 0 & 0 & 1 & 1 & -1 & -1 & 1 & 1 & -1 & -1 \\
0 & 0 & 0 & 0 & 0 & -4 & 4 & 0 & 0 & 0 & 0 & 1 & 1 & -1 & -1 & 1 & 1 & -1 & -1 \\
0 & 2 & 2 & -1 & -1 & -1 & -1 & 1 & 1 & 1 & 1 & 1 & 1 & 1 & 1 & -2 & -2 & -2 & -2 \\
0 & -4 & -4 & 2 & 2 & 2 & 2 & 1 & 1 & 1 & 1 & 1 & 1 & 1 & 1 & -2 & -2 & -2 & -2 \\
0 & 0 & 0 & 1 & 1 & -1 & -1 & 1 & 1 & 1 & 1 & -1 & -1 & -1 & -1 & 0 & 0 & 0 & 0 \\
0 & 0 & 0 & -2 & -2 & 2 & 2 & 1 & 1 & 1 & 1 & -1 & -1 & -1 & -1 & 0 & 0 & 0 & 0 \\
0 & 0 & 0 & 0 & 0 & 0 & 0 & 1 & -1 & -1 & 1 & 0 & 0 & 0 & 0 & 0 & 0 & 0 & 0 \\
0 & 0 & 0 & 0 & 0 & 0 & 0 & 0 & 0 & 0 & 0 & 1 & 1 & -1 & -1 & 0 & 0 & 0 & 0 \\
0 & 0 & 0 & 0 & 0 & 0 & 0 & 0 & 0 & 0 & 0 & 1 & -1 & -1 & 1 & 0 & 0 & 0 & 0 \\
0 & 0 & 0 & 0 & 0 & 0 & 0 & 1 & -1 & 1 & -1 & -1 & 1 & -1 & 1 & 0 & 0 & 0 & 0 \\
0 & 0 & 0 & 0 & 0 & 0 & 0 & -1 & -1 & 1 & 1 & 0 & 0 & 0 & 0 & 1 & -1 & 1 & -1 \\
0 & 0 & 0 & 0 & 0 & 0 & 0 & 0 & 0 & 0 & 0 & 1 & 1 & -1 & -1 & -1 & -1 & 1 & 1
\end{pmatrix},
$$
(13)

and the components of the corresponding moment are

$$
|\mathbf{m}\rangle = (\rho, e, \varepsilon, j_x, q_x, j_y, q_y, j_z, q_z, 3p_{xx}, 3\pi_{xx}, p_{ww}, \pi_{ww}, p_{xy}, p_{yz}, p_{xz}, m_x, m_y, m_z)^T,
$$
(14)

where m_i and π_{ii} are the cubic- and fourth-order polynomials of the momentum, respectively. Note that $p_{ww} = p_{yy} - p_{zz}$ and $\pi_{ww} = \pi_{yy} - \pi_{zz}$. The equilibria of the moments are the functions of the conserved moments and given as

$$
m_0^{eq} = \rho,\ m_1^{eq} = -11\rho + \frac{19}{\rho_0}(j_x^2 + j_y^2 + j_z^2), m_2^{eq} = \omega_\varepsilon \rho + \frac{\omega_{\varepsilon j}}{\rho_0}(j_x^2 + j_y^2 + j_z^2),
$$
(15)

$$
m_{3,5,7}^{eq} = j_{x,y,z}, m_{4,6,8}^{eq} = -\frac{2}{3}j_{x,y,z}, m_9^{eq} = \frac{1}{\rho_0}(2j_x^2 - j_y^2 - j_z^2), m_{10}^{eq} = \omega_{xx}m_9^{eq},
$$
(16)

$$
m_{11}^{eq} = \frac{1}{\rho_0}(j_y^2 - j_z^2),\quad m_{12}^{eq} = \omega_{xx}m_{11}^{eq}, m_{13}^{eq} = \frac{1}{\rho_0}j_x j_y, m_{14}^{eq} = \frac{1}{\rho_0}j_y j_z,
$$
(17)

$$
m_{15}^{eq} = \frac{1}{\rho_0}j_z j_x,\quad m_{16,17,18}^{eq} = 0.
$$
(18)

To recover the corresponding lattice BGK model, the parameters need to be $\omega_\varepsilon = 3$, $\omega_{xx} = -1/2$, $\omega_{\varepsilon j} = -11/2$. However, d'Humieres, Ginzburg, Krafczyk, Lallemand and Luo (2002) recommended their optimized parameters: $\omega_\varepsilon = 0$, $\omega_{xx} = 0$, $\omega_{\varepsilon j} = -475/63$ through the linear analysis for stability of Lallemand and Luo (2000) and thus those parameters are applied in this study.

For the D2Q9 model, the collision matrix is written as

$$
\widehat{\mathbf{S}} = diag(s_0, s_1, \cdots, s_{Q-1}) = diag(s_\rho, s_e, s_\varepsilon, s_j, s_q, s_j, s_q, s_v, s_v),
$$
(19)

and for the D3Q19 model, it is

$$\widehat{\mathbf{S}} = diag(s_\rho, s_e, s_\varepsilon, s_j, s_q, s_j, s_q, s_j, s_q, s_v, s_\pi, s_v, s_\pi, s_v, s_v, s_v, s_m, s_m, s_m),$$ (20)

where the subscript of the relaxation rates corresponds to the physical significance. The kinetic viscosity $v = \mu/\rho$ and the bulk viscosity ζ are given as

$$v = c_s^2 \left(\frac{1}{s_v} - \frac{1}{2} \right) \delta t,$$ (21)

$$\zeta = \frac{c_s^2}{2} \left(\frac{1}{s_e} - \frac{1}{2} \right) \delta t,$$ (22)

where s_v is the relaxation rate for the moments related to the stress and s_e is the relaxation rate for the moment related to the energy. By the gas kinetic theory the mean free path is

$$\lambda = \frac{\mu}{p} \sqrt{\frac{\pi RT}{2}},$$ (23)

and thus with $p = \rho RT = \rho c_s^2$ Eq.(21) can be rewritten as

$$s_v^{-1} = \frac{1}{2} + \frac{\mu}{p\delta t} = \frac{1}{2} + \sqrt{\frac{2}{\pi}} \frac{H \mathrm{Kn}}{c_s \delta t}.$$ (24)

Although the relaxation time: $\tau_i = s_i^{-1}$ is around 1.0, there are several recommended combinations by the pioneering studies [Lallemand and Luo (2000); d'Humieres, Ginzburg, Krafczyk, Lallemand and Luo (2002); etc.]. The present study thus follows some of those as $s_\rho = s_j = 1.0$, $s_e = 1.19$, $s_\varepsilon = 1.4$, $s_\pi = s_\varepsilon$ and $s_m = 1.98$. The relaxation rate s_q is determined through the discussions of the wall boundary condition for non-continuum gas flows.

2.2 Diffusive bounce-back wall boundary condition

The non-slip wall boundary conditions used in the continuum LBM are based on perfect reflection, so the velocity and the temperature of a wall are not reflected into the distribution of the reflected particles. However, from a microscopic viewpoint, the wall boundary condition should include the physics on the wall because the fluid and the wall molecules are interacted with each other. Therefore, the incident particles are modeled to be reflected with the information of the Maxwell distribution function at the wall boundary. The modeled form called the *diffuse scattering* boundary condition is written in the LBM frame as

$$f_\alpha(\mathbf{x},t) = \frac{\sum'_\alpha |(\xi'_\alpha - \mathbf{u}_w) \cdot \mathbf{n}| f'_\alpha(\mathbf{x},t)}{\sum'_\alpha |(\xi'_\alpha - \mathbf{u}_w) \cdot \mathbf{n}| f'^{eq}_\alpha(\mathbf{x},t)} f^{eq}_{\alpha,w}(\mathbf{x},t) := f^D_\alpha(\mathbf{x},t),$$

if

$$\left[(\xi'_\alpha - \mathbf{u}_w) \cdot \mathbf{n} < 0; \ (\xi_\alpha - \mathbf{u}_w) \cdot \mathbf{n} > 0\right], \tag{25}$$

where $\mathbf{n}$ is the unit wall normal vector, ξ'_α is the velocity of incident particles, $f^{eq}_{\alpha,w}$ is the wall equilibrium distribution function, and the subscripts w, α', α respectively denote the wall and the directions of the incident and reflected particles.

The present study applies the *diffusive bounce-back* boundary condition that is the combination of the above diffuse-scattering and bounce-back boundary conditions for the wall boundary as

$$f_\alpha(\mathbf{x}, t + \delta t) = (1 - r) \ f_\beta(\mathbf{x}, t) + r \ f^D_\alpha(\mathbf{x}, t + \delta t), \tag{26}$$

where r is a probability coefficient taking $r = 0.0 - 1.0$, the bounce-back vectors are $\xi_\beta = -\xi_\alpha$ and f^D_α is the diffuse scattering model given by Eq.(25). This model turns into the diffuse scattering model when $r \Rightarrow 1$, whilst it becomes the (non-slip) bounce-back model with $r = 0$. With the analytical consideration of the slip-flow described in section 2.3, the probability coefficient r can be determined.

2.3 Analytical consideration of the slip-flow by the diffusive bounce-back wall boundary condition

2.3.1 Second-order slip-flow model

In a fully developed 2-D Poiseuille flow at the slip flow regime, by integrating the momentum equation with the second order boundary condition

$$u|_{wall} = C_1 \lambda \ \left.\frac{\partial u}{\partial y}\right|_{wall} - C_2 \lambda^2 \ \left.\frac{\partial^2 u}{\partial y^2}\right|_{wall}, \tag{27}$$

the velocity profile can be obtained as

$$\frac{u}{U_c} = 4\frac{y}{H} \left(1 - \frac{y}{H}\right) + \frac{U_s}{U_c}, \tag{28}$$

where H is the channel height, U_c is the centerline velocity: $U_c = aH^2/(8\nu)$, a is the acceleration corresponding to the body force and U_s is the slip velocity at the wall:

$$U_s/U_c = 4C_1 \mathrm{Kn} + 8C_2 \mathrm{Kn}^2. \tag{29}$$

There have been many proposals for the coefficients C_1 and C_2 by the researchers.

The MRT LBM with the diffusive bounce-back wall boundary condition describes the velocity at near wall lattice node 2 as

$$u_2 = A_1 u_1 + A_2 \delta t a, \tag{30}$$

where u_1 is the velocity at lattice node 1. When lattice nodes 1 and 2 are located at $\delta x/2$ and $3\delta x/2$ from the wall (the wall is situated at the half way between nodes 0 and 1), Chai, Shi, Guo and Lu (2010) derived the parameters A_1 and A_2 as

$$A_1 = \frac{3 - 2r + r\tau_v}{1 - r + r\tau_v}, \quad A_2 = \frac{r(11/2 - 2\tau_q - 8\tau_v + 4\tau_q\tau_v) + 4(\tau_q + \tau_v) - 8\tau_q\tau_v - 5}{(2\tau_v - 1)(1 - r + r\tau_v)}, \tag{31}$$

where $\tau_v = s_v^{-1}$ and $\tau_q = s_q^{-1}$. Substituting Eq.(28) into Eq.(30) produces

$$\begin{aligned}
U_s/U_c &= \frac{4r}{2-r}\left(\tau_v - \frac{1}{2}\right)\frac{\delta x}{H} + \frac{16(\tau_q - 1/2)(\tau_v - 1/2) - 3}{3}\left(\frac{\delta x}{H}\right)^2, \\
&= \frac{4r}{2-r}\sqrt{\frac{6}{\pi}}\text{Kn} + \frac{2}{\pi}\frac{16(\tau_q - 1/2)(\tau_v - 1/2) - 3}{(\tau_v - 1/2)^2}\text{Kn}^2.
\end{aligned} \tag{32}$$

Equations (29) and (32) should be the same, then we can obtain

$$r = \frac{2C_1}{\sqrt{\frac{6}{\pi}} + C_1}, \tag{33}$$

$$\tau_q = \frac{1}{2} + \frac{3 + \pi(2\tau_v - 1)^2 C_2}{8(2\tau_v - 1)}. \tag{34}$$

For this second-order slip-flow condition, Chai, Shi, Guo and Lu (2010) employs the coefficients recommended by Hadjiconstantinou (2003): $C_1 = 1.11$, $C_2 = 0.61$.

2.3.2   1.5-order slip-flow model

Mitsuya (1993) derived the second-order slip velocity using the gas kinetic theory [e.g. Bird (1994)] as

$$u|_{wall} = \frac{2}{3}\frac{2 - \alpha}{\alpha}\lambda \left.\frac{\partial u}{\partial y}\right|_{wall} - \frac{1}{2}\left(\frac{2}{3}\lambda\right)^2 \left.\frac{\partial^2 u}{\partial y^2}\right|_{wall}, \tag{35}$$

where α is the accommodation coefficient. Using the nonequilibrium molecular velocity, Kennrd (1938) noted that the momentum transfer produced by the velocity

gradient was nearly $15\pi/32 \approx 3/2$ times larger than that given by the classic gas kinetic theory. Mitsuya (1993) thus multiplied the first term of Eq.(35) by 3/2. When $\alpha = 1$ for a fully diffusive wall, the equation becomes

$$u|_{wall} = \lambda \left. \frac{\partial u}{\partial y} \right|_{wall} - \frac{2}{9} \lambda^2 \left. \frac{\partial^2 u}{\partial y^2} \right|_{wall}. \tag{36}$$

Although it is the second order, Mitsuya named Eq.(36) the 1.5-order slip-flow model. This 1.5-order slip-flow model corresponds to Eq.(27) with $C_1 = 1.0$, $C_2 = 2/9$.

2.3.3 First-order slip-flow model

Verhaeghe, Luo and Blanpain (2009) applied only the first order terms of Eqs (29) and (32) and their expression for r was

$$1 - r = \frac{3\mu - \mathrm{Kn}Hc\rho_0}{3\mu + \mathrm{Kn}Hc\rho_0}, \tag{37}$$

where $c = \delta x/\delta t$. (With Eq.(23) and $p = \rho RT = \rho c_s^2 = \rho/3$, Eq.(33) can be rewritten as Eq.(37) when $c = C_1$.) With this first order slip velocity condition, Verhaeghe, Luo and Blanpain (2009) applied

$$s_q = \frac{8(2 - s_v)}{8 - s_v}, \tag{38}$$

following Ginzbourg and Adler (1994). (In Eq.(32) with $r = 0$, it is recognized that this condition guarantees $U_s = 0$ by the pure bounce-back boundary condition.)

2.4 Interpolated boundary condition

Peng and Luo (2008) concluded that the accuracy of the interpolated bounce-back (IBB) boundary condition was better than that of the immersed-boundary method. Although they chose the quadratic IBB, there wasn't significant difference between the quadratic and linear IBB in Pan, Luo and Miller (2006). Thus, in the present study, the linear IBB is applied. Figs.2(a)-(c) illustrates the procedures of the linear IBB boundary condition of Pan, Luo and Miller (2006) in a one-dimensional setting. As shown in Fig.2(a), in the case that the boundary x_W is located at the middle between nodes x_A and x_B, ($q = |x_A - x_W|/|x_A - x_B| = 1/2$), the particle at node x_A travels and collides with the wall at x_W and reverses its momentum (the collision process completes instantly), then travels back to x_A. Thus, the incoming distribution function is simply equal to the corresponding outgoing one with the opposite momentum. This is so-called half-way bounce-back (HWBB) condition

and accurate in this case. The IBB condition, thus, generalizes the HWBB condition. When $q < 1/2$ as in Fig.2(b), the particle at x_A should end up at x_C after the streaming-collision cycle. Likewise, the particle starting from x_C ends up at x_A after the streaming-collision cycle. This is accomplished by interpolating the distribution function for x_C before the streaming-collision process with the wall takes place. Similarly, when $q > 1/2$, the incoming distribution function can be obtained by using the outgoing one located at x_C after the streaming-collision interaction with the wall takes place and the distribution function values at nearby nodes x_D and x_E as in Fig.2(c). Thus, following Pan, Luo and Miller (2006), the linear IBB formulae for $f_L(x_A, t_{n+1}) = \hat{f}_R(x_C, t_n)$ may be written as

$$f_L(x_A, t_{n+1}) = \begin{cases} (1-2q)f_R(x_A, t_{n+1}) + 2q\hat{f}_R(x_A, t_n), & q < 1/2 \\ \left(1 - \frac{1}{2q}\right)\hat{f}_L(x_A, t_n) + \frac{1}{2q}\hat{f}_R(x_A, t_n), & q \geq 1/2 \end{cases} \tag{39}$$

where f and $\hat{f}$ respectively denote the post- and pre-collision states of the distribution function. The subscripts L and R indicate left- and right-bound directions, respectively.

In order to represent the curved surfaces, an interpolation scheme is also applied to the diffuse scattering boundary condition which is named as the interpolated diffuse scattering (IDS) boundary condition. As schematically shown in Fig.2(d), the distribution functions can be interpolated as

$$f_R(x_W, t_{n+1}) = q f_R(x_A, t_n) + (1-q)f_R(x_D, t_n), \tag{40}$$

$$f_L(x_A, t_{n+1}) = q f_L(x_W, t_n) + (1-q)f_L(x_W, t_{n+1}). \tag{41}$$

Therefore, the interpolation method for the diffusive bounce-back boundary condition consists of the combination of the IBB and the IDS schemes.

2.5 Correction of the molecular mean free path

In microscale wall bounded geometries, the mean free path of the total molecules in the system should be smaller than that in the unbounded systems due to the wall effects. Stops (1970) then introduced a correction function $\Psi(\text{Kn})$ to the molecular mean free path as.

$$\lambda^* = \lambda \Psi(\text{Kn}), \tag{42}$$

where Kn is still the conventional Knudsen number without considering the wall effects. However, as in our previous study [Suga, Takenaka, Ito, Kaneda, Kinjo and
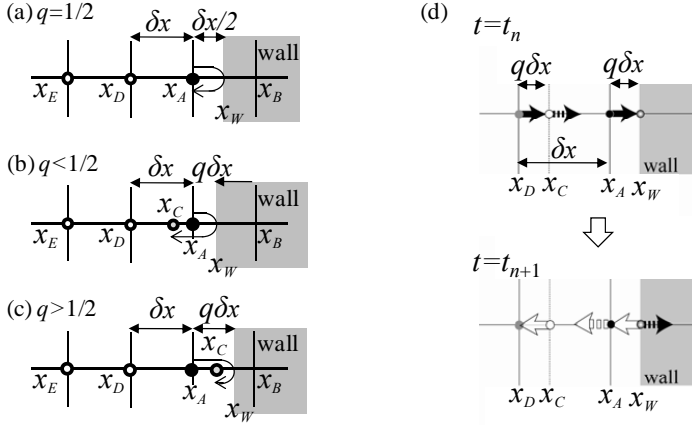
Figure 2: Interpolated bounce-back and diffuse scattering boundary conditions; (a)-(c) linear IBB scheme, (d) linear IDS scheme.

Hyodo (2010)], it can be defined using the local density to include local effects as

$$\text{Kn}^* = \frac{\mu}{\rho H}\sqrt{\frac{\pi}{2RT}}. \tag{43}$$

The function Ψ derived by Stops was very complicated and difficult for particular applications, Guo, Zhao and Shi (2006) thus approximated Stops' function by a simple formula as

$$\Psi(x) = \frac{2}{\pi}\arctan(\sqrt{2}x^{-3/4}), \tag{44}$$

where $x = \text{Kn}^*$. The functional behavior (Ψ decreases as Kn^* increases) indicates that some molecules will hit walls and their flight time may be shorter than the mean free time defined in an unbounded system. Therefore, Eq.(24) may be corrected as

$$s_v^{-1} = \frac{1}{2} + \sqrt{\frac{2}{\pi}}\frac{H\text{Kn}\Psi(\text{Kn}^*)}{c_s\delta t}. \tag{45}$$

2.6 Regularization procedure

Generally speaking, the distribution function **f** has an aliasing error because it cannot be entirely projected on to the Hermite space. Such an error is usually very small, but it can be no longer neglected when the system is far from equilibrium because of high Knudsen number effects. To resolve this problem, the regularization procedure was introduced for improving numerical stability [Zhang, Shang

and Chen (2006)]. The procedure is implemented as the following. First, the distribution function **f** is divided as

$$|\mathbf{f}(\mathbf{x},t)\rangle = |\mathbf{f}^{eq}(\mathbf{x},t)\rangle + |\mathbf{f}'(\mathbf{x},t)\rangle, \tag{46}$$

where **f**′ is the non-equilibrium part of the distribution. Second, it is necessary to convert **f**′ to a new distribution $\tilde{\mathbf{f}}'$ which lies within the subspace spanned by the higher-order Hermite polynomials. Using the Hermite polynomials, the component of $\tilde{\mathbf{f}}'$ is expressed for the D2Q9 or D3Q19 model as

$$\tilde{f}'_\alpha = \omega_\alpha \left[\frac{1}{2c_s^2} H^{(2)} \left(\frac{\boldsymbol{\xi}_\alpha}{c_s} \right) \sum_{\alpha=o}^{Q-1} f'_\alpha \xi_{\alpha i} \xi_{\alpha j} \right], \tag{47}$$

where, $H^{(2)}(x)$ is the second-order Hermite polynomial of a variable x. By replacing **f** in the rewritten Eq.(1):

$$|\mathbf{f}(\mathbf{x}+\boldsymbol{\xi}_\alpha \delta t, t + \delta t)\rangle = |\mathbf{f}(\mathbf{x},t)\rangle - \mathbf{M}^{-1}\widehat{\mathbf{S}}\mathbf{M} \left[|\mathbf{f}(\mathbf{x},t)\rangle - |\mathbf{f}^{eq}(\mathbf{x},t)\rangle \right] \delta t + |\mathbf{F}\rangle \delta t, \tag{48}$$

with Eq.(46) after converting **f**′ of Eq.(46) to $\tilde{\mathbf{f}}'$ by Eq.(47), one can obtain the following form:

$$|\mathbf{f}(\mathbf{x}+\boldsymbol{\xi}_\alpha \delta t, t + \delta t)\rangle = |\mathbf{f}^{eq}(\mathbf{x},t)\rangle + |\tilde{\mathbf{f}}'(\mathbf{x},t)\rangle - \mathbf{M}^{-1}\widehat{\mathbf{S}}\mathbf{M} |\tilde{\mathbf{f}}'(\mathbf{x},t)\rangle \delta t + |\mathbf{F}\rangle \delta t. \tag{49}$$

This regularization process enforces the system to be confined within the second-order Hermite moment space filtering out all the higher-order nonequilibrium contributions from numerical lattice artifacts which contaminate the solutions.

3   Molecular Dynamics Method

In this study, a flow around a triangular prism situated in a nanochannel and a bumpy channel flow are simulated by the MD method to generate reference data for validating the LBMs.

MD simulations solve classical equations of the motions of *N*molecules interacting via model potentials. Although several model potentials have been proposed, the present study applies the simplest and the most frequently used Lennard-Jones 6-12 potential. The Lennard-Jones 6-12 potential is defined as

$$\phi(r) = 4\varepsilon \left[\left(\frac{\sigma}{r} \right)^{12} - \left(\frac{\sigma}{r} \right)^6 \right], \tag{50}$$

where r is the intermolecular distance, ε and σ are the well depth and the diameter of the molecules. The earliest MD simulation for the properties of argon applied this model potential. In the system which is modeled by the Lennard-Jones molecules only, the classical equation of motion can be rewritten as

$$\frac{d^2r^*}{dt^{*2}} = -\frac{\varepsilon\tau^2}{m\sigma^2}\frac{\partial\phi^*}{\partial r^*}, \tag{51}$$

where m, $r^* = r/\sigma$, $t^* = t/\tau (= t/\sqrt{m\sigma^2/\varepsilon})$ and $\phi^* = \phi/\varepsilon$ are the mass, the nondimensional length, time and energy, respectively. However, to make a physical interpretation, it is sometimes expressed as finite values in terms of argon. In addition, the nondimensional number density $N^*(= N\sigma^3)$ and temperature $T^*(= k_BT/\varepsilon) = 2.0$ are used in the Lennard-Jones fluid. (Here k_B is the Boltzmann constant.)

In order to enhance the computational efficiency of the interactions, the potential effects beyond a cut off distance $r_c = 2.5\sigma - 5.5\sigma$ are normally truncated. In the present study, $r_c = 3.0\sigma$ is applied.

3.1 Structure of wall molecules

In the case of fluid flows in a finite space surrounded by walls, the flow is governed by the interaction between the fluid and wall molecules. Thus, it is inevitable to evaluate the flow phenomena in terms of the intermolecular potential energy between the fluid and the wall which varies by the system structure and properties. Thompson and Troian (1997) modeled the walls of the Couette flow by molecules arranged on (111) planes of a face-centered cubic (fcc) lattice. Li (2009) discussed the mechanism of friction-induced fluid heating in Poiseuille flows considering the walls of four layers of molecules arranged on fcc lattice sites. Liu and Li (2009) discussed the fluid-wall interaction artificially changing the fluid-wall binding energy. In our previous studies [Suga, Takenaka, Ito and Kaneda (2010); Suga, Takenaka, Ito, Kaneda, Kinjo and Hyodo (2010)], in order to reduce the computational load, the wall was simulated by an argon atom monolayer. By this wall model, obstacles such as the square cylinder are represented by rolled mono-layers.

In this study, however, in order to consider the effects of the structure inside the solid wall regions, the wall molecules are arranged on the fcc lattice and the wall surfaces are formed by its (111) planes as shown in Fig.3. The distance between the centers of neighboring molecules is set to σ. Each of the wall molecules is tethered to fixed lattice site locations by harmonic springs with a large spring constant. Since the present cut off distance is $r_c = 3.0\sigma$, three layers of argon molecules are considered to form the walls. With this situation, the fluid-wall interaction is artificially tuned by adjusting the well depth of the Lennard-Jones potential to be 0.75 (multiply Eq.(50) by 0.75). As shown in Fig.4, comparing the simulation results

with those of the DSMC [Beskok and Karniadakis (1999))] of the fully diffusive walls where the accommodation coefficient is $\alpha = 1$, the present MD simulation code well reproduces the flow filed at Kn = 0.06 - 0.22. Here, streamwise velocity U is normalized by the bulk velocity U_b. (See Suga, Takenaka, Ito, Kaneda, Kinjo and Hyodo (2010) for the way of obtaining the Kn in the MD simulation.)
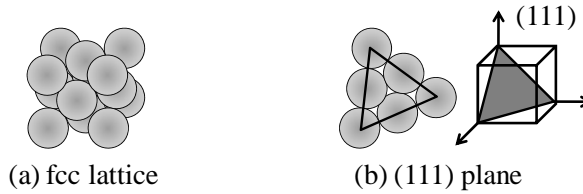

(a) fcc lattice   (b) (111) plane

Figure 3: (a) Face-centered cubic crystal lattice and (b) surface orientation of the (111) plane of the fcc crystal.
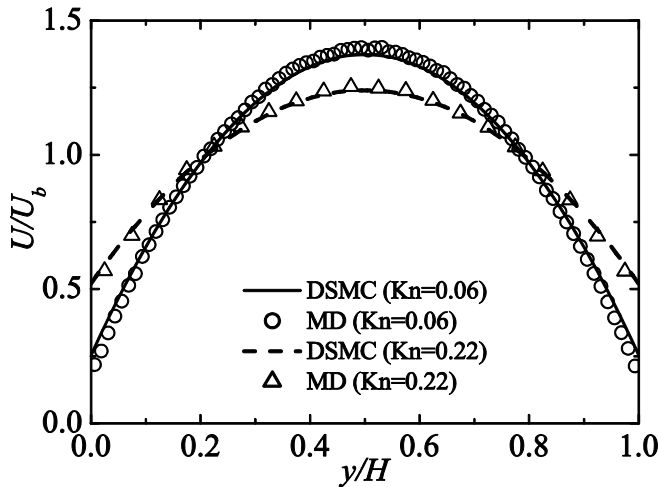
Figure 4: Comparison of the velocity profiles by the present MD simulation code with those of DSMC in force driven Poiseuille flows at different Knudsen numbers.

4   Results and Discussions

Simulations of canonical force-driven Poiseuille flows are firstly discussed and then, triangular-cylinder flow and the square-cylinder flow are discussed. Finally,

a 3-D bumpy channel flow is discussed comparing with the result of the presently performed MD simulation.

4.1 *Force-driven Poiseuille flows*

Figure 5 compares the velocity profiles of plane Poiseuille channel flows at Kn=0.01-10 with the data of the DSMC of Beskok and Karniadakis (1999). These velocity profiles are normalized by the bulk velocity U_b. The 2-D uniform Cartesian lattice of 100×100 is used for the simulations. This density of the lattice was confirmed to be more than fine enough by our previous study [Niu, Hyodo, Munekata and Suga (2007)]. The number of iterations of the LBM simulations is 1,000-5,000 and the results are fully converged. (For the lower Kn case, the larger iteration times are required.) The compared LBMs are the MRT LBMs by the first-order, 1.5-order and the second-order slip-flow models.

All the velocity profiles are accurate enough at Kn≤ 0.1 and there is almost no difference between the models compared. However, as in our previous study [Suga, Takenaka, Ito, Kaneda, Kinjo and Hyodo (2010)], it is recognizable that the near wall profiles at Kn≥ 1 are not very accurate by the D2Q9 model. (The difference between the predictions and the reference data is up to 20% at the wall at Kn=10.) This tendency is confirmed in Fig.6(a) which compares the slip and centerline velocities: U_s and U_c. Although each agreement is not good enough, the profiles of U_s and U_c by the first-order slip-flow model correspond best to the reference data [Karniadakis, Beskok and Aluru (2005); Ohwada, Sone and Aoki (1989)] and those by the second-order slip-flow model are the worst among the profiles at Kn> 0.1. However, as shown in Fig.6(b), for the mass flow rate:

$$Q = \sum_{y=0}^{H} \rho U(y)/(\rho a H^2/c_s),\qquad(52)$$

the 1.5-order slip-flow model leads to the best agreement among the slip-flow models. Interestingly, each profile shown in Fig.6(b) corresponds well to the analytically obtained distributions plotted in figure 4 of Mitsuya (1993).

Only the different points in the model terms are the values of the probability coefficient r and the relaxation time τ_q for the energy flux. By Eq.(33), the probability coefficient is fixed as $r = 0.84, 0.84$ or 0.89 by the first-order, 1.5-order or second-order slip-flow model, respectively. The relaxation time τ_q varies a lot depending on the Knudsen number. At Kn=0.01, $\tau_q = 0.64, 0.88$ or 1.29 whilst it is 0.50, 239.26 or 655.96 at Kn=10 by the first-order, 1.5-order or second-order slip-flow model, respectively, when the channel height is divided into 99 lattice spaces. Consequently, at Kn≪0.1, the difference in the values of r or τ_q is not significantly large

and this results in the nearly the same results of the flow characteristics. However, at Kn»1, the difference in the values of τ_q becomes very large and accordingly it affects the predicted behavior such as the flow rate shown in Fig.6(b).

In order to assess the merits of the correction of the molecular mean free path $\lambda^* = \lambda\Psi$, Figs. 7 and 8 compare the results of the MRT μ-flow LBMs incorporated with the slip-flow models and the correction: $\lambda^* = \lambda\Psi$. (The notation $+\Psi$ means that Eq.(45) is used instead of Eq.(24).) By comparing Fig.7 with Fig.5, it is readily recognizable that improvement is obvious for the prediction at Kn=1 and 10. Indeed, the discrepancy between the velocity by the first-order slip-flow model and the reference data reduces to 5% at the wall. This is also confirmed in Fig.8(a) which indicates general improvement of the prediction at Kn>0.1. The improvement by the correction of the molecular mean free path is more obviously seen in the flow rate profiles shown in Fig.8(b). By comparing Figs.6(b) and 8(b), it is recognizable that the correction of the mean free path reduces the flow rate error of each slip-flow model. In particular, the error reduces from 75% to 15% at Kn=10 in the 1.5-order slip-flow model.

Figure 9 indicates the effects of the regularization procedure. Although the general predictive tendencies in Figs.9(a) and (c) are similar to those shown in Figs.5(d) and 6(a), interestingly, with the regularization procedure, all the slip-flow models produce nearly the same flow characteristics even at Kn>1. This means that with the regularization, the order of the slip-flow model may not be very important. Since the regularization filters out higher-order numerical lattice artifacts and systematically incorporates the higher-order moments, it can be considered that any difference in the model equations caused by the presently evaluated slip-flow models is corrected along with the other higher-order artifacts implicitly included in the MRT model. The improvement by the correction of the molecular mean free path are also confirmed at Kn>1 as shown in Figs.9(b),(d) and (f). The higher the Kn becomes, the more the correction of the molecular mean free path affects the relaxation time near the wall. In the flow rates, however, by comparing Figs.9(e) and (f), it is recognizable that the general tendencies are not changed very much.

Note that Zhang, Shang and Chen (2006) reported that after the regularization the SRT BGK model with the D2Q9 produced results which were very close to the exact Navier-Stokes theoretical curve up to a significantly high Kn. Their results are far different from our results shown in Fig.9 since they used pure bounce-back wall boundary condition. Indeed, their predicted slip velocities were very low and nearly reaching to zero.
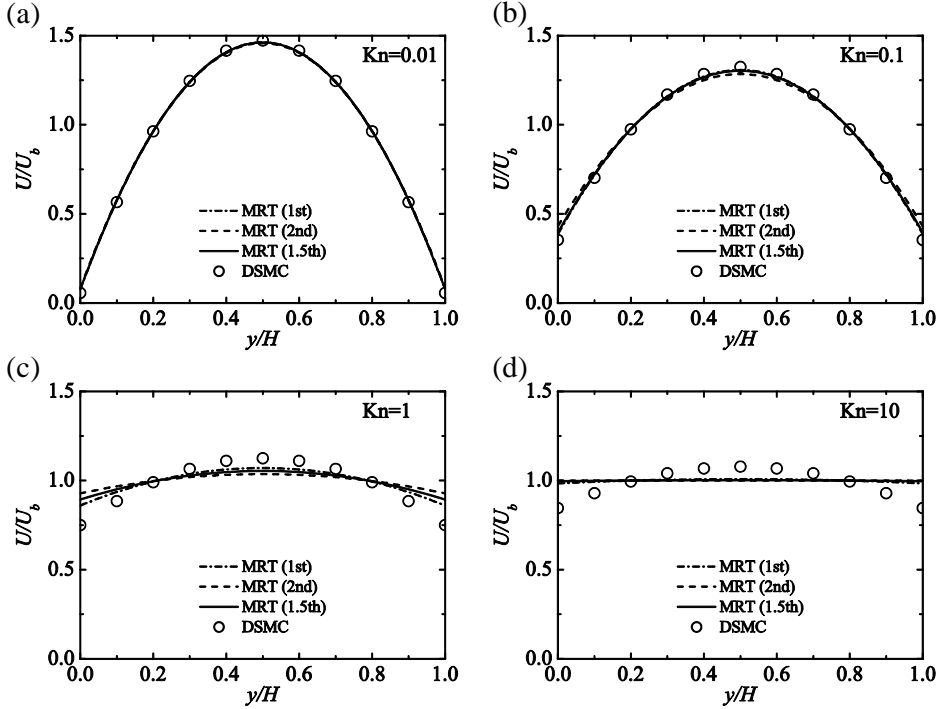
Figure 5: Velocity profile comparisons of the MRT μ-flow LBM with slip-flow models in Poiseuille flows; (a) at Kn=0.01, (b) at Kn=0.1, (c) at Kn=1.0, and (d) at Kn=10; the DSMC data are from Beskok and Karniadakis (1999).

4.2 Triangular-cylinder and square-cylinder flows

As shown in Figs.10(a) and (b), flows in a nanochannel with a triangular-cylinder or a square-cylinder placed in the center region are considered. Periodic boundary condition is applied to the inlet and outlet boundaries and thus, the flow regime is regarded as a part of an infinite cylinder array set in a nanochannel. The force is applied to the *x*-direction only to drive the flow.

In Table 1, the computational conditions for the MD simulation are summarized. The computational domains shown in Fig.11 have sizes of $21\sigma \times 21\sigma \times 17.32\sigma$ and $30\sigma \times 30\sigma \times 20.78\sigma$, respectively for the triangular-cylinder and the square-cylinder flows. In the triangular-cylinder flow, 2,240 fluid molecules surrounded by 3,080 wall molecules are simulated whereas in the square-cylinder flow, 5,376 fluid molecules surrounded by 5,232 wall molecules are simulated in the present study. After the process described in Suga, Takenaka, Ito, Kaneda, Kinjo and Hy-
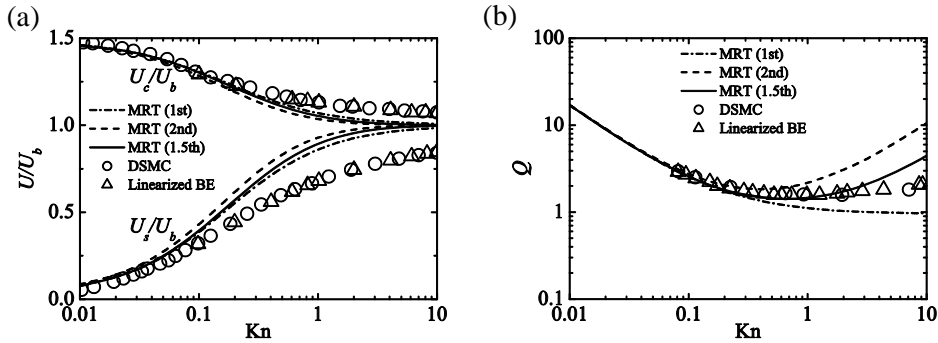
(a)

(b)

Figure 6: Dependency of the flow characteristics on Kn; (a) velocity scaling at wall and centerline of the channels, and (b) flow rate; the DSMC data are from Karniadakis, Beskok and Aluru (2005), the linearized BE data are from Ohwada, Sone and Aoki (1989).

Table 1: Computational conditions of the MD simulation for a flow around an obstacle in a channel.

	domain size	fluid molecules	wall molecules	number density	Kn
triangular-cylinder flow	$21\sigma \times 21\sigma$ $\times 17.32\sigma$	2240	3080	0.3076	0.15
square- cylinder flow	$30\sigma \times 30\sigma$ $\times 20.78\sigma$	5376	5232	0.29936	0.11

odo (2010), the obtained Knudsen numbers from the MD simulation are Kn=0.15 and Kn=0.11, respectively in the triangular- and the square-cylinder flows. To obtain reasonable flow statistics, 8 million time steps are required by the MD simulations. (Note that although the flow geometry of the MD simulation is essentially three dimensional, the statistic flow characteristics are two dimensional in these flow cases. Thus, statistic averaging is performed in the spanwise direction to obtain 2-D flow statistics by the MD simulation.)

The corresponding LBM simulations are thus carried out on the 2-D grids at the corresponding Kn to those of the MD results. The grid sizes are 96×96 and 100×100 for the triangular- and the square-cylinder flows, respectively. As described in our previous study [Suga, Takenaka, Ito, Kaneda, Kinjo and Hyodo (2010)], the order of the grid size: 100×100 was confirmed to be enough for grid independent solutions. The number of iterations of the LBM simulations is 2,000 and the results
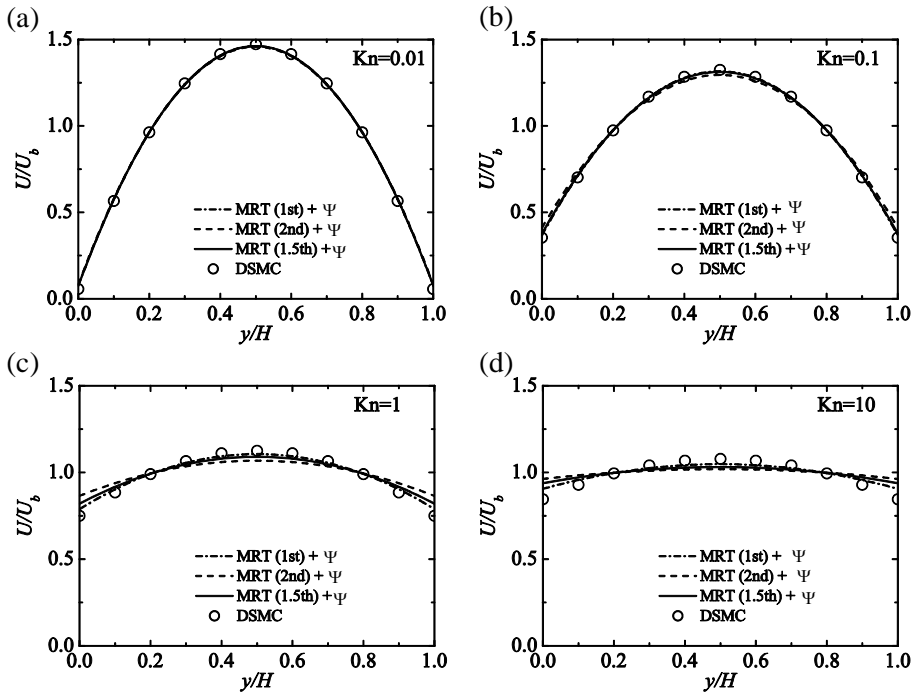
Figure 7: Effects of the correction of the molecular mean free path on velocity profiles; (a) at Kn=0.01, (b) at Kn=0.1, (c) at Kn=1.0, and (d) at Kn=10.
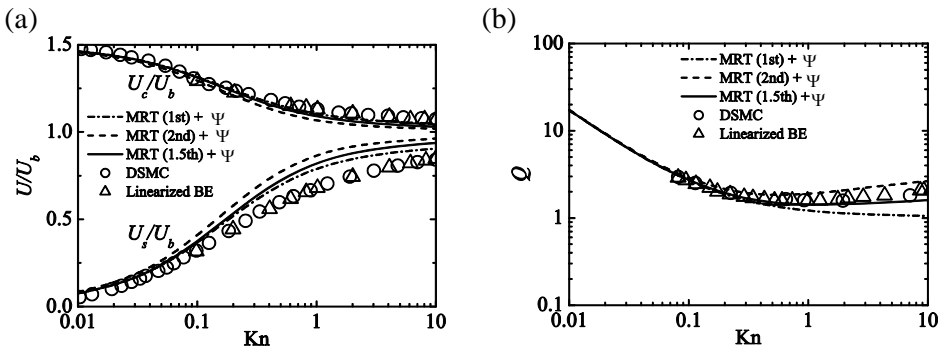

Figure 8: Effects of the correction of the molecular mean flow path on the flow characteristics; (a) velocity scaling at wall and centerline of the channels, (b) flow rate.
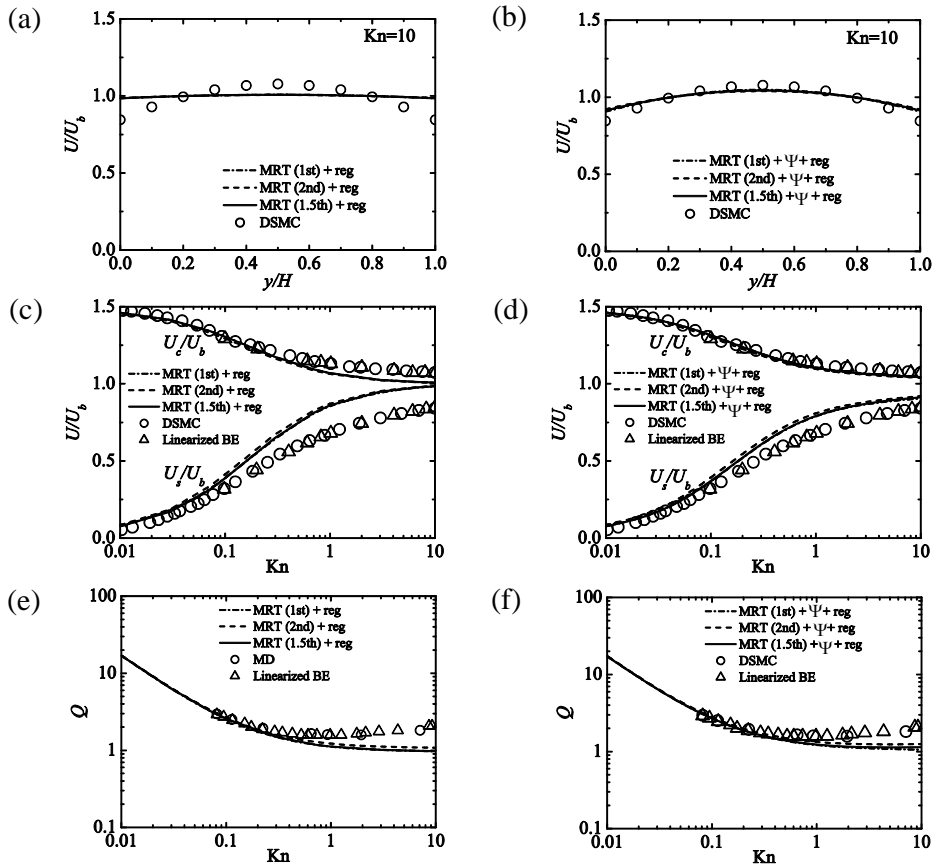
Figure 9: Effects of the regularization on the flow characteristics; (a) velocity profiles at Kn=10, (b) velocity profiles at Kn=10 along with the correction of the molecular mean free path, (c) slip and centerline velocities, (d) slip and centerline velocities along with the correction of the molecular mean free path, (e) flow rates, (f) flow rate along with the correction of the molecular mean free path.

are fully converged.

Figure 12 compares the velocity profiles in the triangular-cylinder flow. As clearly seen in Fig.12(a), without the regularization procedure, although there are slight discrepancies in the profiles by the different orders of the slip-flow models, all the results show reasonable agreement with the MD simulation results. Indeed, it can be observed that the discrepancy between the MRT LBM and the MD results is up to 20% of U_b at the most difficult position to predict. Moreover, with the
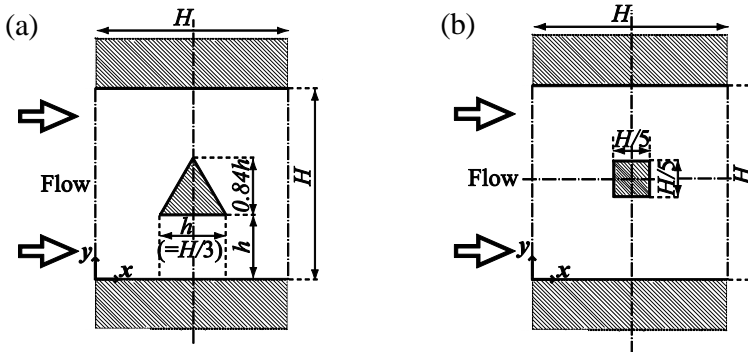
Figure 10: Flow field geometry; (a) triangular-cylinder flow, (b) square-cylinder flow.
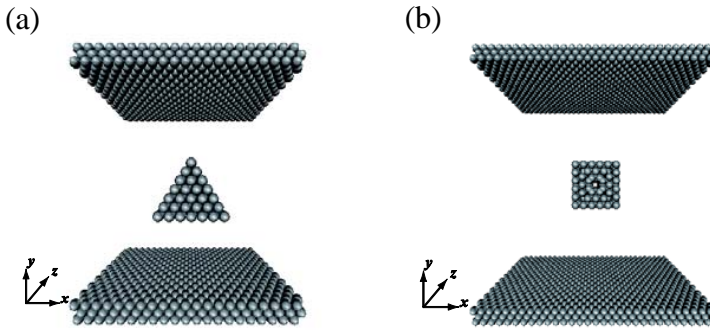

Figure 11: Atomic 3-D views of obstacle flows in the MD simulations; (a) triangular-cylinder flow, (b) square-cylinder flow.

higher-order slip-flow model, the slip velocity at the peak of the triangle tends to be oscillating as noticed in the profiles at $x/H = 0.5$. As reported by our previous study [Suga, Takenaka, Ito, Kaneda, Kinjo and Hyodo (2010)], such oscillations can be dealiased by introducing the regularization procedure. When the projection of the lattice Boltzmann equation into the Hermite space is considered, it is understood that the collision step introduces an error due to the fact that the distribution function does not automatically lie entirely within the Hermite space. In the case that the system is not far from equilibrium, such an error is small and ignorable [Zhang, Shang and Chen (2006)]. (Since the number of the distribution functions is normally greater than that of the flow variables, the set of unknowns can be considered as over-determined and thus non-equilibrium part of the distribution includes higher order moments in principle.) Indeed, with the regularization process,

the oscillations and discontinuity in the profiles disappear as shown in Fig.12(b). Interestingly, all the slip-flow models produce virtually the same velocity profiles as in Figs.12(b) and (c). At this level of Kn, it is readily understandable after the discussions in the Poiseuille flows.

The same tendency is also confirmed in the square-cylinder flow as shown in Fig.13. With the regularization procedure, all the slip-flow models produce almost the same velocity profiles and the agreement between the LBM and the MD results looks ideal. Therefore, in complex micro-flow geometries, the regularization process is very effective for the MRT LBM to damp the oscillations even at Kn<1. Once the regularization process is incorporated, the order of the slip-flow model, which determines the probability coefficient of the diffusive bounce-back condition and the relaxation time for the energy flux, is not very important. Since the considered Knudsen numbers are under Kn=1, the correction of the molecular mean free path does not change the results at all though it is not shown here.

4.3   3-D bumpy channel flow

Figure 14 shows the computational domain and schematic views of the 3-D bumpy channel flow. As shown in Figs.14(a) and (b), matrices of hemisphere bumps are placed on the top and bottom walls in a staggered fashion. The radius of the hemisphere is $R = 0.4H$ where H is the channel height and the pitch of the bumps. Periodic boundary condition is applied to the streamwise (x) and spanwise (z) directions. To drive the fluid, the force is applied to the x-direction only. This flow field is considered to represent some features of the catalytic layer of a fuel cell.

Table 2: Computational conditions of the MD simulation for a flow through a bumpy wall channel.

domain size	fluid molecules	wall molecules	number density	Kn
$20\sigma \times 20\sigma \times 20.78\sigma$	1656	5162	0.2684	0.1

In Table 2, the computational conditions for the MD simulation are summarized. The computational domain shown in Fig.14(c) is $20\sigma \times 20\sigma \times 20.78\sigma$, and 1,656 fluid molecules surrounded by 5,162 wall molecules are simulated. The estimated Knudsen number is Kn=0.1. To obtain reasonable flow statistics, 30 million time steps are required.

The corresponding LBM simulations are carried out on the 3-D grids at the corresponding Knudsen number Kn=0.1. The grid size used is $100 \times 100 \times 100$. As confirmed by our previous study [Suga, Takenaka, Kinjo and Hyodo (2011)], the grid sizes of $100 \times 100 \times 100$ is enough for grid independent solutions in a complex
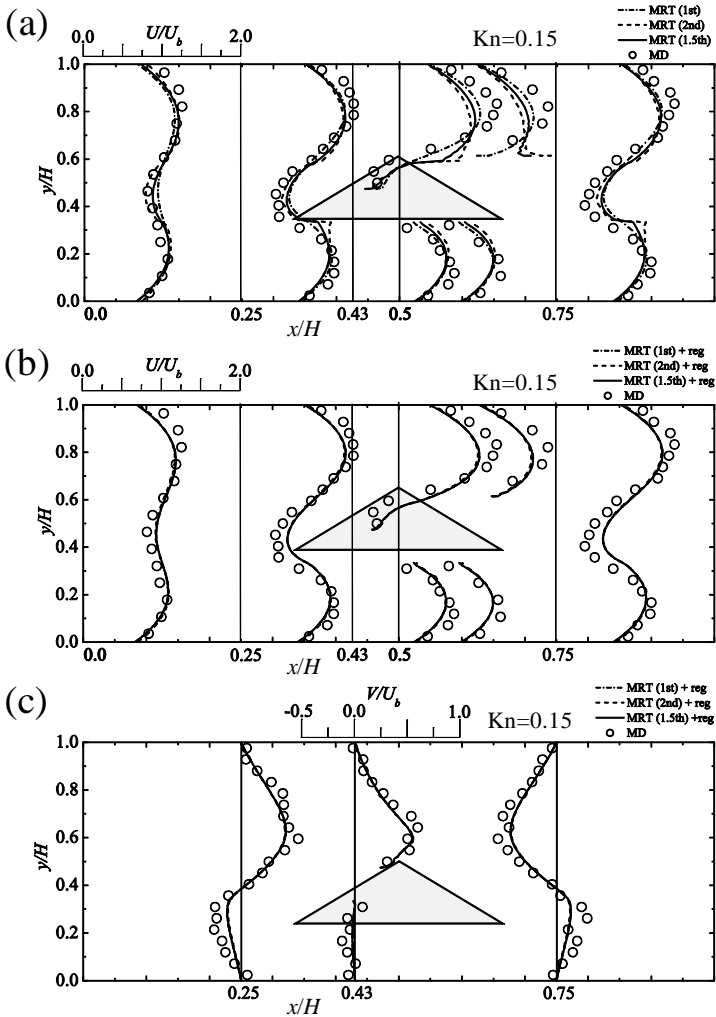
Figure 12: Comparison of velocity profiles around a triangular-cylinder in a nanochannel at Kn=0.15; (a) streamwise velocity component profiles without the regularization process, (b) streamwise velocity component with the regularization process, (c) vertical velocity component with the regularization process.

3-D flow geometry at Kn≈0.1. The number of iterations of the LBM simulations is more than 4,000 and the results are fully converged.

Figure 15 compares velocity profiles at the symmetry plane: $z/H = 0.5$ (Fig.15(a)) and an off-center plane: $z/H = 0.25$ (Figs.15(b)-(d)). As discussed in the 2-D test flow cases, with the regularization procedure, it is clearly seen that all the slip-
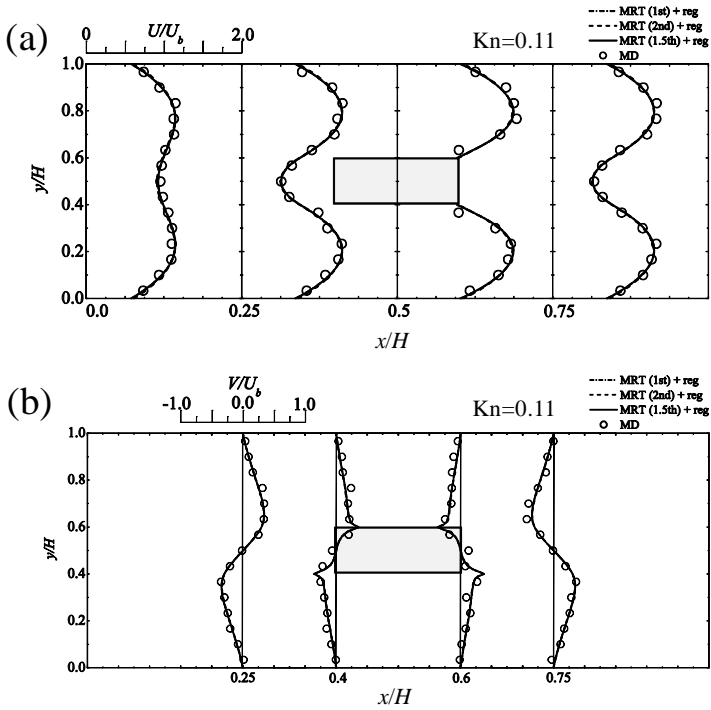
Figure 13: Comparison of velocity profiles with the regularization process around a square-cylinder in a nanochannel at Kn=0.11; (a) streamwise velocity component, (b) vertical velocity component.
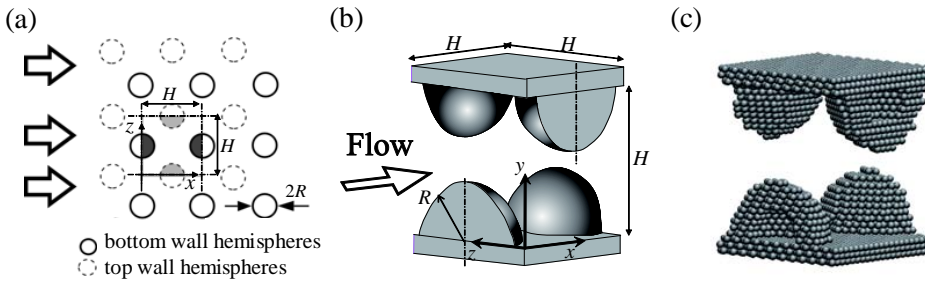

Figure 14: Computational domain of a 3-D bumpy wall channel flow; (a) plane view of the computational domain, (b) schematic view of the flow field, (c) atomic 3-D view of the flow field in the MD simulation.

flow models show the same predictive tendency. Generally, the agreement between the MRT LBM and the MD simulation results is very satisfactory. The maximum discrepancy between the results is indeed up to 15% of the bulk velocity U_b. Since without the regularization procedure, the solution of the MRT LBM by the first-order slip-flow model shows oscillations in the entire flow field, the regularization process does improve the solution stability. However, unlike in the 2-D flows, even with the regularization, somehow kinky profiles still can be seen near walls at some sections such as $x/H =0.1$ and 0.9 in the symmetry plane (Fig.15(a)). Also weak oscillations appear near the bottom wall at $x/H =0.3$ and 0.7 in the plane of $z/H = 0.25$ (Figs.15(b)-(d)).

Since the flow field and characteristics are much more complicated than those of the 2-D test flows, it may not be easy to damp such near-wall kinks or oscillations by the regularization procedure even at Kn=0.1. However, it is worth re-considering the linear interpolation scheme for the diffusive bounce-back boundary condition used in the present study because its accuracy of the curvature representation is only in the first order.

5   Conclusions

In the present study, the MRT μ-flow LBM is extensively discussed through its evaluation in several test flows such as 2-D force-driven Poiseuille flows at $0.01 \leq Kn \leq 10$, flows in a nanochannel with a triangular-cylinder and a square-cylinder placed in the center region at $Kn \approx 0.1$, and a 3-D flow through a bumpy wall channel at Kn=0.1. The main frame of the MRT μ-flow LBM consists of the multiple relaxation time LBM with the second-order D2Q9 or D3Q19 discrete velocity model and the diffusive bounce-back wall boundary condition. The probability coefficient of the diffusive bounce-back condition and the relaxation time for the energy flux are obtained by the slip-flow model in the modified Reynolds equation of tribology. In the Poiseuille flows at Kn>1, the set of coefficients obtained by referring to the 1.5-order slip-flow model leads better flow rates than those by the first- and second-order models. The near wall correction of the molecular mean free path improves the results particularly at Kn>1. The regularization procedure to remove the aliasing error generally improves the prediction. For the 2-D and 3-D complex flows the regularization procedure is essential to stabilize the solution results. With the regularization procedure, the coefficients by the first- to second-order slip-flow models hardly affect the simulation results. Since the regularization filters out higher-order numerical lattice artifacts and systematically incorporates the higher-order moments, it is considered that any difference caused by the slip-flow model is corrected along with the other higher-order artifacts implicitly included in the MRT model. The results of the MRT μ-flow LBM with the regularization proce-
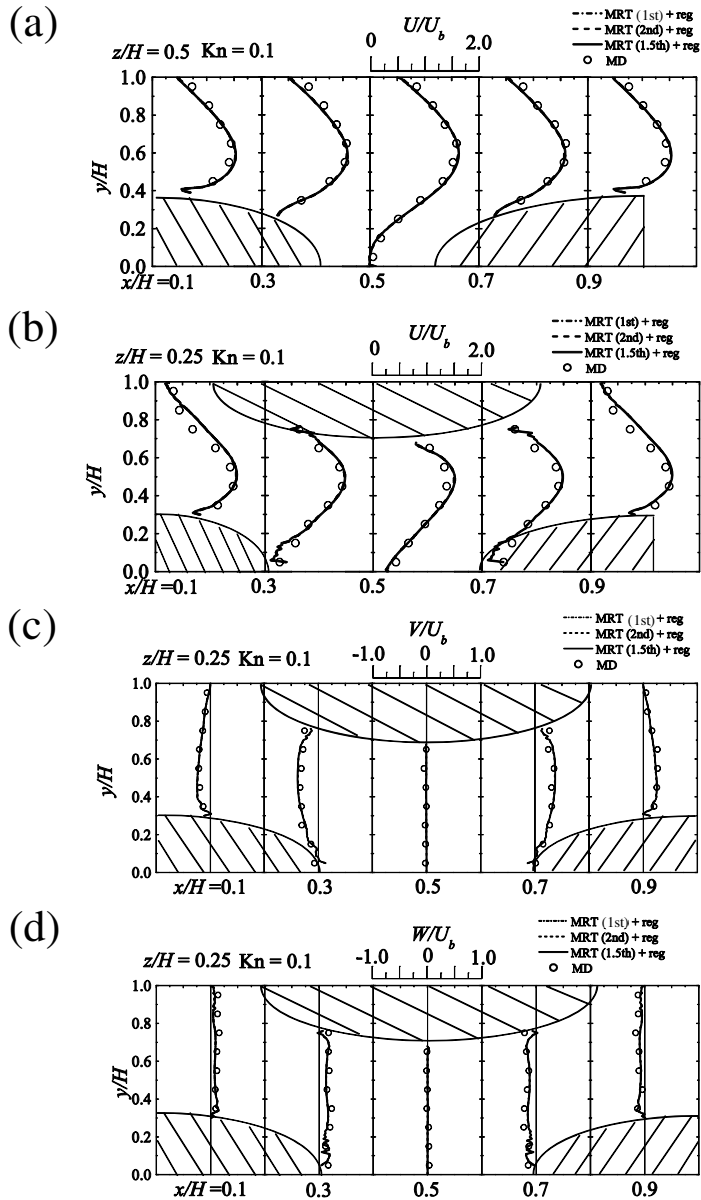
Figure 15: Comparison of velocity profiles with the regularization procedure in a 3-D bumpy channel at Kn=0.1; (a) streamwise velocity component at $z/H = 0.5$, (b) streamwise velocity component at $z/H = 0.25$, (c) vertical velocity component at $z/H = 0.25$, (d) spanwise velocity component at $z/H = 0.25$.

dure hence agree very well with the reference data of the 2-D cylinder flows and the 3-D bumpy channel flow at Kn≈0.1. It is concluded that introducing the regularization procedure is very effective for simulating micro flows by the MRT LBM even with the second order discrete velocity models.

References

Ansumali, S.; Karlin, I. V. (2002): Kinetic boundary conditions in the lattice Boltzmann method. *Phys. Rev. E*, vol.66, 026311.

Beskok, A.; Karniadakis, G.E. (1999): A model for flows in channels, pipes and ducts at micro- and nano-scales. *Nanoscale Microscale Thermophys. Eng.*, vol.3, pp.43-77.

Bhatnagar, P.L.; Gross, E.P.; Krook, M. (1954): A model for collision processes in gases. Small amplitude processes in charged and neutral one-component systems. *Phys. Rev.*, vol.94, pp. 511-525.

Bird, G.A. (1994): *Molecular gas dynamics and the direct simulation of gas flows*. Clarendon Press, Oxford.

Bocquet, L.; Barrat, J.L. (1993): Hydrodynamic boundary conditions and correlation functions of confined fluids. *Phys. Rev. Lett.*, vol.70, pp.2726-2729.

Cercignani, C. (1975): *Theory and Application of the Boltzmann Equation,* Scottish Academic Press.

Chai, Z.; Shi, B.; Guo, Z.; Lu, J. (2010): Gas flow through square array of circular cylinders with Klinkenberg effect: A lattice Boltzmann study. *Commun, Comput. Phys.*, vol. 8, pp. 1052-1073.

Chapman, S.; Cowling, T.G. (1970): *The Mathematical Theory of Non-Uniform Gases,* Cambridge University Press, Cambridge, England .

d'Humieres, D.; Ginzburg, I.; Krafczyk, M.; Lallemand, P.; Luo, L.-S. (2002): Multiple-relaxation-time lattice Boltzmann models in three dimensions. *Philos. Trans. R. Soc. London, Ser. A* , vol.360, pp.437-451.

Ginzbourg, I; Adler, P.M. (1994): Boundary flow condition analysis for the three-dimensional lattice Boltzmann model. *J. Phys. II France*, vol.4, pp.191-214.

Guo, Z.-L.; Zhao, T.-S.; Shi, Y. (2006): Physical symmetry, spatial accuracy, and relaxation time of the lattice Boltzmann equation for micro gas flows. *J. Appl Phys.*,

vol.99, 074903.

Guo, Z.; Zheng, C.; Shi, B. (2008): Lattice Boltzmann equation with multiple effective relaxation times for gaseous microscale flow. *Phys. Rev. E*, vol.77, 036707.

Hadjiconstantinou, N.G. (2003): Comment on Cercignani's second-order slip coefficient. *Phys. Fluids*, vol.15, pp.2352-2354.

Haile, J. (1997): *Molecular Dynamics Simulation: Elementary Methods*. John Wiley & Sons Inc.

Higuera, F. J.; Jimenez, J. (1989): Boltzmann Approach to Lattice Gas Simulations. *Europhys. Lett.*, vol.9, pp.663-668.

Karniadakis, G.; Beskok, A.; Aluru, N. R. (2005): *Microflows and Nanoflows: Fundamentals and Simulation*, Springer.

Keehm, Y.; Mukerji, T.; Nur, A. (2004): Permeability prediction from thin sections: 3D reconstruction and lattice-Boltzmann flow simulation. *Geophys. Res. Lett.*, vol.31, L04606.

Kennard, E.H. (1938): *Kinetic Theory of Gases,* McGraw-Hill, pp. 145-147.

Klinkenberg, L.J. (1941): The permeability of porous media to liquids and gases. in *Drilling and Production Practice*, American Petroleum Inst., pp.200-213.

Koplik, J.; Banavar, J.R. (1995): Continuum deductions from molecular hydrodynamics. *Ann. Rev. Fluid Mech.*, vol.27, pp.257-292.

Lallemand, P.; Luo, L.-S. (2000): Theory of the lattice Boltzmann method: Dispersion, dissipation, isotropy,Galilean invariance, and stability. *Phys. Rev. E*, vol.61, pp.6546-6562.

Li, Z. (2009): Surface effects on friction-induced fluid heating in nanochannel flows. *Phys. Rev. E*, vol.79, 026312.

Liu, C.; Li, Z. (2009): Flow regimes and parameter dependence in nanochannel flows. *Phys. Rev. E*, vol.80, 036302.

McNamara, G. R.; Zanetti, G. (1988): Use of the Boltzmann equation to simulate lattice-gas automata. *Phys. Rev. Lett.* vol. 61, pp. 2332-2335.

Mitsuya, Y. (1993): Modified Reynolds equation for ultra-thin film gas lublication using 1.5-order slip-flow model and considering surface accommodation coefficient. *J. Tribology*, vol. 115, pp. 289-294.

Nie, X.; Doolen, G. D.; Chen, S. (2002): Lattice-Boltzmann simulations of fluid flows in MEMS. *J. Statistical Phys.*, vol.107, pp.279-289.

Niu, X.-D.; Hyodo, S.; Munekata, T.; Suga, K. (2007): Kinetic lattice Boltzmann method for microscale gas flows: Issues on boundary condition, relaxation time, and regularization. *Phys. Rev. E*, vol.76, 036711.

Niu, X.-D.; T. Munekata, T.; Hyodo, S.; Suga, K. (2007): An investigation of water-gas transport processes in the gas-diffusion-layer of a PEM fuel cell by a multiphase multiple-relaxation-time lattice Boltzmann model. *J. Power Sources*, vol.172, pp.542-552.

Ohwada, T.; Sone, Y.; Aoki, K. (1989): Numerical analysis of the shear and thermal creep flows of a rarefied gas over a plane wall on the basis of the linearized Boltzmann equation for hard-sphere molecules. *Phys. Fluids A*, vol.1,pp.1588-1599.

Pan, C.; Luo, L.-S.; Miller, C.T. (2006): An evaluation of lattice. Boltzmann schemes for porous medium flow simulation. *Comput. Fluids*, vol.35, pp. 957–965.

Peng, Y.; Luo, L.-S. (2008): A comparative study of immersed-boundary and interpolated bounce-back methods in LBE. *Progr. Comput. Fluid Dyn.*, vol.8, pp.156-167.

Sbragaglia, M.; Succi, S. (2005): Analytical calculation of slip flow in lattice Boltzmann models with kinetic boundary conditions. *Phys. Fluids*, vol.17, 093602.

Shen, **C.**; **Tian**, **D. B.**; **Xie**, **C.**; **Fan**, **J.** (2004): Examination of the LBM in simulation of microchannel flow in transitional regime. *Microscale Thermophys. Eng.*, vol.8, pp.423-432.

Stops, D. W. (1970): The mean free path of gas molecules in the transition regime. *J. Phys. D*, vol.3, pp.685-696.

Succi, S. (2002): Mesoscopic modeling of slop motion at fluid-solid interfaces with heterogeneous catalysis. *Phys. Rev. Lett.*, vol.89, 064502.

Suga, K.; Ito, T. (2010): Lattice Boltzmann flow models for micro/nano fluidics, *CMES: Computer Modeling in Engineering and Sciences*, vol.63, pp. 223-242.

Suga, K.; Nishio, Y. (2009): Three dimensional microscopic flow simulation across the interface of a porous wall and clear fluid by the lattice Boltzmann method. *The Open Transp. Phenom. J.*, vol.1, pp.35-44.

Suga, K.; Takenaka, S.; Ito, T.; Kaneda, M. (2010): Lattice Boltzmann flow simulation in a combined nanochannel. *Adv. Appl. Math. Mech.*, vol.2 , pp.609-625.

Suga, K.; Takenaka, S.; Ito, T.; Kaneda, M.; Kinjo, T.; Hyodo, S. (2010): Evaluation of a lattice Boltzmann method in a complex nanoflow. *Phys. Rev. E*, vol.82, 016701.

Suga, K.; Takenaka, S.; Kinjo, T.; Hyodo, S. (2011): Simulation of 3-D nano-mesh flows by a micro-flow LBM and its evaluation against the MD simulations, *Prog. Comput. Fluid Dyn.*, vol.11, pp. 139-148.

Suga, K.; Tanaka, T.; Nishio, Y.; Murata, M. (2009): A boundary reconstruction scheme for lattice Boltzmann flow simulation in porous media. *Prog. Comp. Fluid Dyn.*, vol.9, pp. 201-207.

Thompson, P.A. ; Troian, S.M. (1997): A general boundary condition for liquid flow at solid surfaces. *Nature*, vol.389, pp.360-362.

Toschi, F.; Succi, S. (2005): Lattice Boltzmann method at finite Knudsen numbers. *Europhys. Lett.*, vol.69, pp.549-555.

Verhaeghe, F.; Luo, L.-S.; Blanpain, B. (2009): Lattice Boltzmann modeling of microchannel flow in slip flow regime. *J. Comput. Phys.*, vol.228, pp.147-157.

Zhang, Y.-H.; Gu, X.-J.; Barber, R.W. ; **Emerson, D.R.** (2006): Capturing Knudsen layer phenomena using a lattice Boltzmann method. *Phys. Rev. E*, vol.74, 046704.

Zhang, Y.-H.; Qin, R.; Emerson, D.R. (2005): Lattice Boltzmann simulation of rarefied gas flows in microchannels. *Phys. Rev. E*, vol.71, 047702.

Zhang, R.; Shang, X.; Chen, H. (2006): Efficient kinetic method for fluid simulation beyond the Navier-Stokes equation. *Phys. Rev. E*, vol.74, 046703.